

Mapping the surface phase diagram of GaAs(001) using droplet epitaxy

C. X. Zheng,^{1,2} K. Hannikainen,³ Y. R. Niu,^{3,4} J. Tersoff,⁵ D. Gomez,³ J. Pereiro,³ and D. E. Jesson^{3,*}

¹School of Science, Westlake University, Hangzhou 310024, Zhejiang Province, China

²Institute of Natural Sciences, Westlake Institute for Advanced Study, Hangzhou 310024, Zhejiang Province, China

³School of Physics and Astronomy, Cardiff University, Cardiff CF24 3AA, United Kingdom

⁴MAX IV Laboratory, Lund University, Fotongatan 2, 22484 Lund, Sweden

⁵IBM T. J. Watson Research Center, Yorktown Heights, New York 10598, USA



(Received 2 October 2019; published 26 December 2019)

We combine droplet epitaxy with low-energy electron microscopy imaging techniques to map the surface phase diagram of GaAs(001). The phase patterns produced in droplet epitaxy are interpreted using a simple model which links the spatial coordinates of phase boundaries to the free energy. It is thereby possible to gain important information on surface phase stability, based on the observed sequential order of the phases away from the droplet edge. This can be used to augment existing $T = 0$ K phase diagrams generated by density-functional theory calculations. We establish the existence of a (3×6) phase, and confirm that the controversial (6×6) phase is thermodynamically stable over a narrow range of chemical potential.

DOI: 10.1103/PhysRevMaterials.3.124603

I. INTRODUCTION

Droplet epitaxy [1–3] has emerged as a flexible technique for growing quantum dots and more complex nanostructures [4–11]. In this approach, liquid droplets of group-III metal are first deposited on a III–V semiconductor surface, for example Ga on GaAs(001). Then exposure to a group-V flux, such as As₄, results in the formation of an epitaxial GaAs quantum structure.

In this paper we adapt droplet epitaxy as a tool for mapping the surface phase diagram of GaAs(001), by combining it with advanced low-energy electron microscopy imaging [12]. The GaAs(001) surface is of great importance for electronic applications and has been intensively studied over the years (see, e.g., Refs. [13–25]). Surface phases of differing structure and composition are used in the growth of optoelectronic materials, InGaAs quantum devices, and dilute magnetic semiconductors by molecular-beam epitaxy (MBE). This has led to significant efforts to understand and control the stability of surface phases as a function of experimental conditions. The conventional approach is to calculate the Gibbs surface free energy as a function of Ga surface chemical potential μ_{Ga} (or equivalently As chemical potential μ_{As} , since the sum is fixed [26,27]). Then μ_{Ga} (or μ_{As}) can be related to experimental conditions (see, for example [23,26]). However, μ_{Ga} is difficult to control experimentally since it depends sensitively on temperature [28] and material deposition [29]. Recently, efforts have been made to control μ_{Ga} by slowly varying the substrate temperature in the presence of liquid droplets [30]. This facilitated the study of the phase diagram in the Ga-rich limit. However, key questions still remain regarding phase stability across the wider range of μ_{Ga} , extending towards and including the As-rich regime.

During droplet epitaxy there is a gradient of surface chemical potential with distance from the Ga droplet. Using low-energy electron microscopy (LEEM) we can directly observe a sequence of distinct surface phases reflecting the varying chemical potential. By determining which phases occur, and their ordering with chemical potential, we can map out the surface phase diagram across a wide range of continuously varying μ_{Ga} at fixed temperature. In this way we establish the existence of a (3×6) phase. Additional experiments, combined with theoretical modeling of the chemical potential gradient, allow us to confirm that the controversial (6×6) phase is thermodynamically stable over a narrow range of chemical potential. These phases are absent in the theoretical $T = 0$ K phase diagram, and we discuss how thermal effects may stabilize them at experimental temperatures.

It should be emphasized that although we apply a combination of LEEM and droplet epitaxy to specifically study the GaAs(001) surface, the methods presented here are quite general and are highly complementary to density-functional theory (DFT) calculations. As such, we believe this specific study points the way to mapping surface phase diagrams across a wide range of material systems. This includes other technologically important III–V compounds, such as nitrides.

II. SAMPLE PREPARATION

Experiments were performed in an ultrahigh-vacuum (UHV) LEEM specially modified for III–V MBE [31]. Temperatures were measured using an infrared pyrometer calibrated to the congruent evaporation temperature of 625 °C [27,29]. This involved a correction due to the T dependence of the surface emissivity [32]. An undoped GaAs(001) sample was degassed at 300 °C for 24 h and then annealed at 580 °C for 2 h to remove the surface oxide. Ga droplets of radius $\sim 1 \mu\text{m}$ were prepared by annealing above the congruent evaporation temperature at 650 °C, and the droplets were

*dej.workaddress@gmail.com

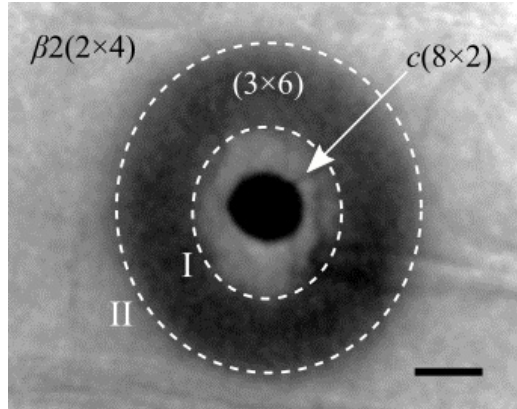


FIG. 1. Droplet epitaxy phase pattern (DEPP) of GaAs(001). The bright-field contrast spatially separates surface phases surrounding a central droplet. The scale bar corresponds to 2 μm .

allowed to run across the surface [28,33], creating smooth planar (001) regions which we utilize for our droplet epitaxy imaging experiments [34]. In particular cases (e.g., Fig. 1) droplet motion was used to smooth the entire surface.

III. RESULTS AND DISCUSSION

A. Droplet epitaxy phase patterns

Figure 1 contains a bright field LEEM image of a Ga droplet on GaAs(001) under an As_4 flux of 10^{-5} Torr beam effective pressure (BEP) at 550 °C. Surrounding the droplet is a stationary, dark concentric ring enclosed by boundaries I and II. This is slightly elliptical, due to anisotropic surface diffusion on GaAs (001) and the contrast is linked to the spatial variation in surface phases which produce variations in incident electron reflectivity (see, for example, Ref. [35]). We term this contrast variation a droplet epitaxy phase pattern (DEPP). Microspot low-energy electron diffraction (μ LEED) identifies the inner bright region as $c(8 \times 2)$, the outer bright region as $\beta2(2 \times 4)$, and the dark ring itself as a (3×6) surface reconstruction. However, as we show below, boundary I is also associated with a narrow region of (6×6) phase.

To explain the origin of this phase pattern and establish the link to surface free energy, we consider a simple model for DEPP formation. The Ga droplet acts as a source of Ga adatoms which interact with the surface and any As adatoms. To evaluate the Ga adatom concentration surrounding the droplet, let us consider a random array of droplets of radius r_D (assumed constant throughout the course of the experiment), with typical nearest-neighbor distance $2L$ (with $L \gg r_D$). The droplet array is subjected to an As flux F_{As} and the reaction-diffusion equation for the Ga concentration outside the droplet at radial coordinate r and time t is

$$\frac{\partial C_{\text{Ga}}}{\partial t} = D_{\text{Ga}} \left(\frac{\partial^2 C_{\text{Ga}}}{\partial r^2} + \frac{1}{r} \frac{\partial C_{\text{Ga}}}{\partial r} \right) - k_r [C_{\text{Ga}} C_{\text{As}} - (C_{\text{Ga}} C_{\text{As}})_{eq}] \quad (1)$$

Here, C_{As} and C_{Ga} are the respective As and Ga surface adatom concentrations and D_{Ga} is the Ga diffusion coefficient. k_r is a reaction rate constant governing the reaction between As and Ga to form GaAs solid and $(C_{\text{Ga}} C_{\text{As}})_{eq}$ is the adatom

concentration product in equilibrium with the solid. We neglect Ga adatom desorption into the vacuum. As a reasonable approximation, Eq. (1) assumes radial symmetry and we impose the boundary condition $\partial C_{\text{Ga}}/\partial r = 0$ at $r = L$, since the concentration is symmetric halfway between the droplets.

Above 350 °C, the As residence time τ_{As} is short [36], much shorter than other relevant time scales. Compared to desorption, reaction with Ga is only a small perturbation (which we neglect) to the As concentration. We therefore treat the As density as uniform, with steady-state value $C_{\text{As}} = F_{\text{As}} \tau_{\text{As}}$ for sufficiently large flux F_{As} . Furthermore, we can assume it comes instantly into steady state with flux (on a time scale τ_{As}). This is equivalent to $\tau_{\text{As}} \ll \tau_{\text{Ga}} = 1/(k_r C_{\text{As}})$ where τ_{Ga} is the Ga adatom mean lifetime before reaction with As.

If $L_{\text{Ga}} = \sqrt{D_{\text{Ga}} \tau_{\text{Ga}}}$ is the Ga diffusion length, then for $L \gg L_{\text{Ga}}$, one can show that the steady-state solution to Eq. (1), i.e., with $\partial C_{\text{Ga}}/\partial t = 0$, is $C_{\text{Ga}}(r) = BK_0(r/L_{\text{Ga}}) + (C_{\text{Ga}} C_{\text{As}})_{eq}/F_{\text{As}} \tau_{\text{As}}$ where B is a constant for given temperature T and flux F_{As} (see Appendix A). Here, K_0 is a modified Bessel function of the second kind [37]. In the limit of fast attachment, the droplet shrinkage is diffusion limited and $C_{\text{Ga}}|_{r=r_D} = C_{\text{Ga}}^l$ where C_{Ga}^l is the Ga adatom concentration in equilibrium with the liquid Ga droplet. Using the relationship between the surface adatom concentration and chemical potential, $\mu_{\text{Ga}} = E_{\text{Ga}} + kT \ln(C_{\text{Ga}}/\nu_{\text{Ga}})$ [38], the Ga chemical potential at radial position r and temperature T , for flux F_{As} is simply

$$\mu_{\text{Ga}}(r) = E_{\text{Ga}} + kT \ln \left(\frac{BK_0(r/L_{\text{Ga}})}{\nu_{\text{Ga}}} + \frac{(C_{\text{Ga}} C_{\text{As}})_{eq}}{\nu_{\text{Ga}} F_{\text{As}} \tau_{\text{As}}} \right), \quad (2)$$

which is plotted in Fig. 2(a). Here, k is Boltzmann's constant and we assume the Ga adatoms may sit at ν_{Ga} equivalent surface sites per unit area, of energy E_{Ga} . For simplicity, we neglect vibrational entropy contributions.

The droplet therefore acts as a source of Ga adatoms which react with As to form GaAs. This results in a monotonically decreasing Ga chemical potential as a function of radial distance from the droplet edge, as illustrated in Fig. 2(a). The spatial phase pattern observed in Fig. 1 can now be explained using this simple model, as follows. First consider a radial position r_c associated with the boundary between phases α and β , as represented schematically in Fig. 2(a). Such a boundary might approximate experimental boundaries I or II in Fig. 1, for example. This is associated with a chemical potential $\mu_{\text{Ga}}(r_c)$ such that the surface free energies [per (1×1) cell] of the two phases are equal,

$$G_\alpha[\mu_{\text{Ga}}(r_c)] = G_\beta[\mu_{\text{Ga}}(r_c)], \quad (3)$$

as shown schematically in Fig. 2(b). Thus, the real-space position of phase boundaries around droplets can be used to map surface free energies as a function of chemical potential.

DEPPs, as contained in Fig. 1, provide a continuously varying [39] and monotonically decreasing μ_{Ga} and are, therefore, a valuable tool for carefully and extensively exploring μ_{Ga} phase space. However, we can also improve the resolution of the technique in μ_{Ga} by utilizing the time dependence of DEPP formation. Establishing a steady-state reaction-diffusion field surrounding the droplet takes a finite time after turning the As flux on or off. This creates a time-

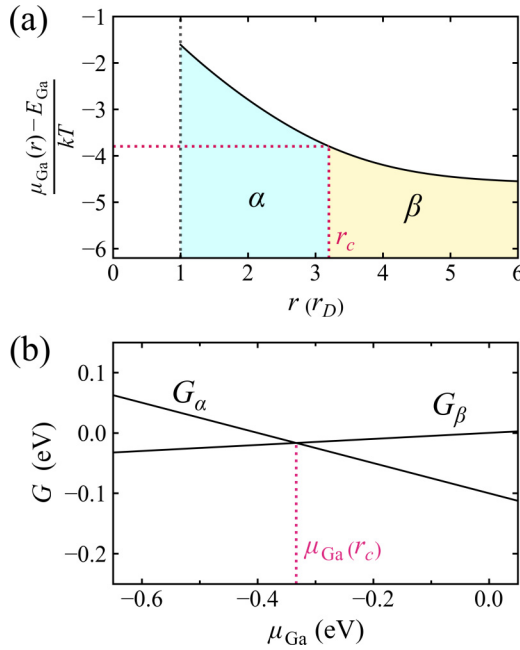


FIG. 2. (a) Ga chemical potential at radial position r away from the droplet edge located at r_D . For illustration we have taken $C_{\text{Ga}}^l/\nu_{\text{Ga}} = 0.2$, $C_{\text{Ga}}^L/\nu_{\text{Ga}} = 0.01$, and $r_D/L_{\text{Ga}} = 1$ (see Appendix A). (b) Schematic representation of the free energy G [per (1×1) unit cell] of phases α and β plotted as a function of μ_{Ga} . The phases have the same free energy at $\mu_{\text{Ga}}(r_c)$ corresponding to radial position r_c in (a).

dependent chemical potential $\mu_{\text{Ga}}(r, t)$ which can be used to improve the resolution.

B. Time-dependent droplet epitaxy phase patterns; improved resolution

To illustrate the above ideas we consider the time-dependent droplet epitaxy experiment contained in Fig. 3. Panel (a) displays a droplet and smooth planar trail region, created by previous droplet motion, which we utilize for our imaging experiments [34]. The sample is at 550°C with the As shutter closed so that the entire trail region is composed of the $c(8 \times 2)$ phase. Upon opening the As shutter at $t = 0$, boundaries I and II can be seen moving inwards towards the droplet [Fig. 3(b)]. The radial position of boundaries I and II is displayed in Fig. 4(b) as a function of time. At $t = 33$ s they approach their steady-state positions, at which point the As is turned off. The boundaries then move outwards along the trail [Fig. 3(c)], as displayed in Fig. 4(b). An experimental LEEM movie of phase boundary motion dynamics when the As flux is turned on and off, corresponding to the sequence of Fig. 3, is provided in the Supplemental Material [40].

The sequential motion of different phases along the trail enables time-resolved μ LEED data to be obtained. The illumination aperture used to collect μ LEED data can be strategically placed at a given trail position to obtain diffraction information as a function of time. Experimentally, we find that improved chemical potential resolution and phase discrimination occurs when the aperture is placed at a position away from the droplet edge, as indicated in Fig. 3(a). Additionally,

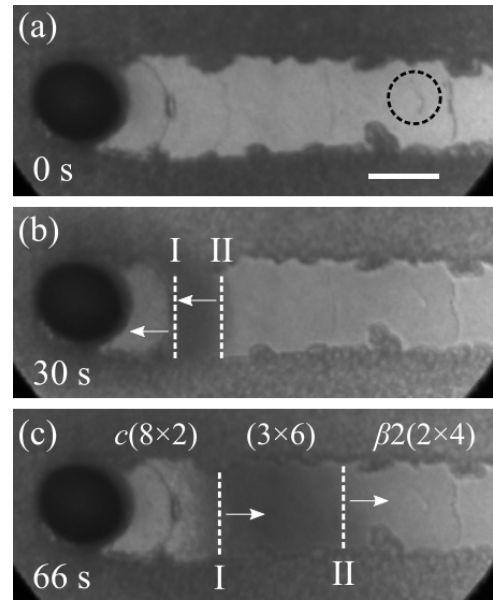


FIG. 3. Bright-field LEEM image of a Ga droplet and smooth trail region of GaAs(001): (a) at $t = 0$ s before the As flux is turned on, (b) 30 s after the As flux is turned on, and (c) 33 s after the As flux is turned off (i.e., 66 s after it was first turned on). The black dashed circle in (a) indicates the position of the illumination aperture, and the scale bar corresponds to $2 \mu\text{m}$. The sample temperature is 550°C .

the time-resolved collection of diffraction data is optimized when the As flux is turned off and the phase boundaries are moving outwards with a slower velocity compared with their inward motion when As is turned on.

Figure 4(a) contains μ LEED diffraction patterns (i)–(iv) obtained from the illumination aperture position indicated in Fig. 3(a). The patterns were collected at corresponding times indicated by the crosses in Fig. 4(b). Schematic diffraction patterns are also shown, where large circles indicate the positions of (1×1) spots. Diffraction patterns (iv), (iii), and (i) correspond to the $\beta 2(2 \times 4)$, (3×6) , and $c(8 \times 2)$ phases, respectively, which is consistent with Fig. 1. However, we detect new diffraction information at time (ii), close to the passing of boundary I. The observed μ LEED diffraction pattern is a superposition of (6×6) and $c(8 \times 2)$ phases as shown in Fig. 4(a), indicating the presence of an additional (6×6) phase in this region.

To understand the phase boundary motion on turning As on and off and the apparent improvement in μ_{Ga} resolution away from the droplet edge, we turn to Eq. (1). Initially, before the As flux is turned on, the surface is in quasiequilibrium with the liquid Ga droplets and the Ga adatom density is equal to C_{Ga}^l across the entire surface. This corresponds to the initial, uniform chemical potential profile $\mu_{\text{Ga}}^0(r) = \mu_{\text{Ga}}^l$ at $t = 0$ as shown in Fig. 5(a) which lies above critical chemical potentials μ_{Ga}^I and μ_{Ga}^{II} (represented by dotted lines), which respectively correspond to boundaries I and II [see Figs. 1 and 3(c)]. Consequently, the entire trail for zero As flux displays the $c(8 \times 2)$ reconstruction [Fig. 3(a)] (see also [30]).

Upon turning on the As flux at $t = 0$, we assume C_{As} increases instantly from its quasiequilibrium value $C_{\text{As}}^0 = (C_{\text{Ga}}C_{\text{As}})_{\text{eq}}/C_{\text{Ga}}^l$ to $F_{\text{As}}\tau_{\text{As}}$ and we solve Eq. (1) for $\mu_{\text{Ga}}(r, t)$

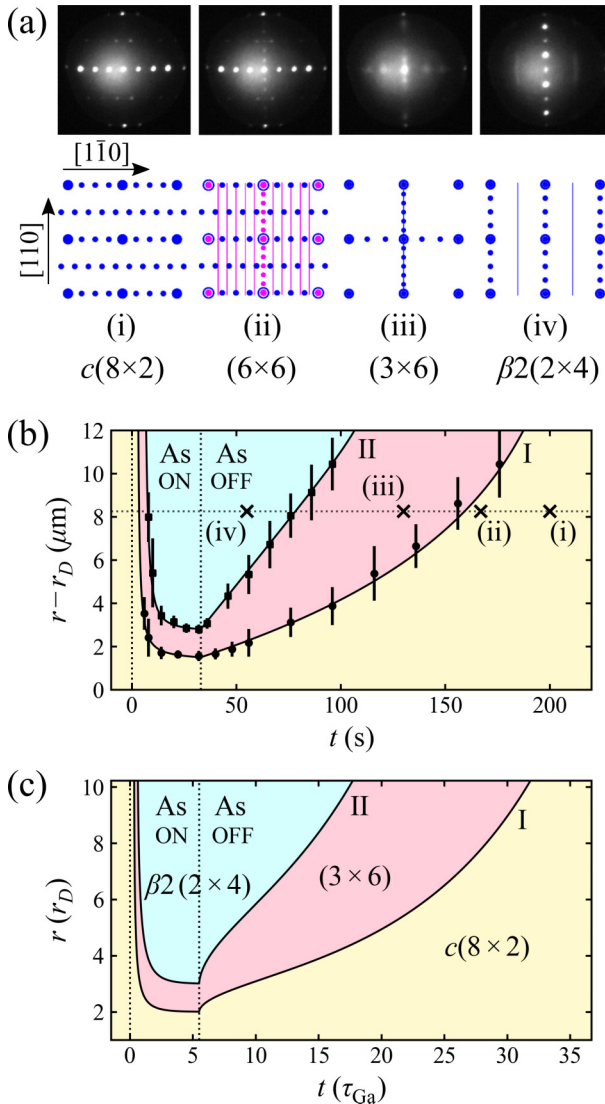


FIG. 4. (a) Time-resolved μ LEED data collected from the illumination aperture shown in Fig. 3(a) located 8 μm from the droplet. Schematic diffraction patterns are also shown, where large circles indicate the positions of (1×1) spots. (b) Measured r vs t trajectories of phase boundaries I and II, when turning the As flux on and off. The horizontal dotted line marks the position of the aperture in Fig. 3(a), with the crosses corresponding to the acquisition times of the LEED data contained in (a). The dotted vertical lines represent the times at which the As shutter was opened and closed. (c) Theoretical trajectories of boundaries I and II calculated from Eq. (1) (see Appendix B). Time is given in units of reaction time $\tau_{\text{Ga}} = (k_r F_{\text{As}} \tau_{\text{As}})^{-1}$, and radial coordinate r is given in droplet radii r_D . The computational parameters are set to the representative values of $C_{\text{Ga}}^l/v_{\text{Ga}} = 0.25$, $C_{\text{Ga}}^L/v_{\text{Ga}} = 5 \times 10^{-3}$, $\rho_D = 0.1$, and $\rho_L = 7$. The chemical potentials defining boundaries I and II give stationary boundary positions at $r_I/r_D = 2$ and $r_{II}/r_D = 3$, respectively.

at later times $t > 0$ (see Appendix B for details and also the Supplemental Material for the movie simulating the time evolution of μ_{Ga} profiles [40]). As displayed in Fig. 5(a), $\mu_{\text{Ga}}(r, t)$ decreases with time as the incoming As reacts with surface Ga, on a time scale determined by the reaction time $\tau_{\text{Ga}} = (k_r F_{\text{As}} \tau_{\text{As}})^{-1}$. Ga is however replenished by the

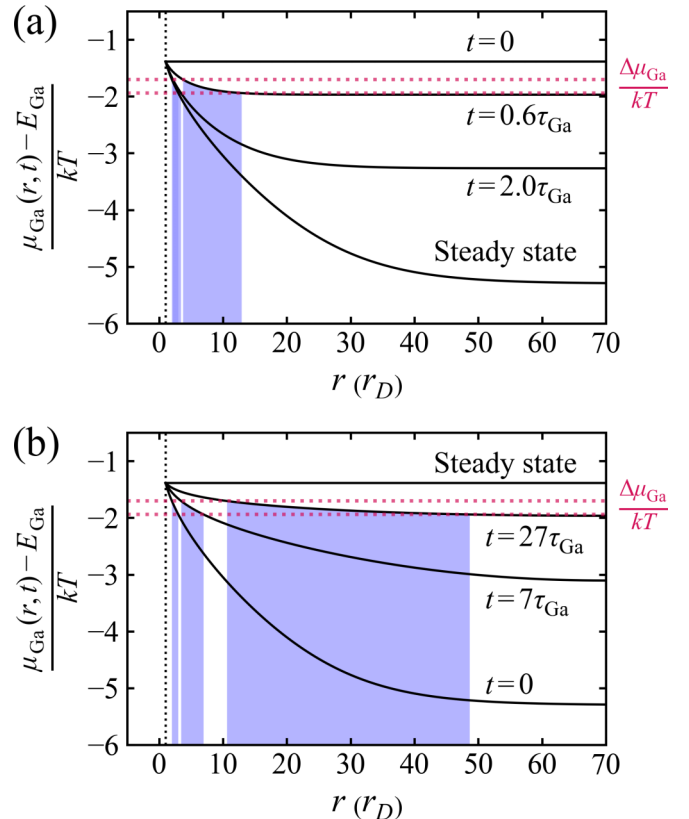


FIG. 5. Ga chemical potential profiles $\mu_{\text{Ga}}(r, t)$ after turning the As flux (a) on, and (b) off. The droplet edge is located at $r = r_D$. The critical chemical potentials μ_{Ga}^I and μ_{Ga}^{II} corresponding to boundaries I and II are represented by the upper and lower horizontal dashed lines, respectively. The shaded regions represent the evolving real-space region Δr corresponding to $\Delta\mu_{\text{Ga}} = \mu_{\text{Ga}}^I - \mu_{\text{Ga}}^{II}$ [each shaded region relates to one instantaneous $\mu_{\text{Ga}}(r, t)$ profile, where time is displayed in units of $\tau_{\text{Ga}} = (k_r F_{\text{As}} \tau_{\text{As}})^{-1}$ in both (a) and (b)]. We set the computational parameters to the representative values of $C_{\text{Ga}}^l/v_{\text{Ga}} = 0.25$, $C_{\text{Ga}}^L/v_{\text{Ga}} = 5 \times 10^{-3}$, $\rho_D = 0.1$, and $\rho_L = 7$ (see Appendix A). The values of μ_{Ga}^I and μ_{Ga}^{II} give stationary boundary positions at $r_I/r_D = 2$ and $r_{II}/r_D = 3$, respectively.

droplet, which pins the chemical potential at the droplet edge. Eventually, $\mu_{\text{Ga}}(r, t)$ crosses μ_{Ga}^I at some distance from the droplet and boundary I appears at radial coordinate r_I such that $\mu_{\text{Ga}}(r_I, t) = \mu_{\text{Ga}}^I$. As $\mu_{\text{Ga}}(r, t)$ decreases with time, r_I and boundary I move inwards toward the droplet. Similarly, at a later time, boundary II appears at r_{II} [where $\mu_{\text{Ga}}(r_{II}, t) = \mu_{\text{Ga}}^{II}$] and also moves inwards along the trail with time. Eventually, both boundaries reach their steady-state positions (cf. Figs 1 and 2) when the steady-state $\mu_{\text{Ga}}(r, t)$ profile is attained.

When the As flux is turned off, we assume that C_{As} goes instantly from $F_{\text{As}} \tau_{\text{As}}$ back to C_{As}^0 , consistent with a small τ_{As} . The initial profile is now the $\mu_{\text{Ga}}(r)$ of Eq. (2), and the C_{As} in Eq. (1) is now $C_{\text{As}} = C_{\text{As}}^0$. As displayed in Fig. 5(b), $\mu_{\text{Ga}}(r, t)$ begins to increase as Ga is supplied from the solid GaAs and the droplets. This causes the phase boundary positions $r_I(t)$ and $r_{II}(t)$ to initially move away from the droplet. Eventually all phase boundaries accelerate and disappear as soon as $\mu_{\text{Ga}}(r, t)$ exceeds μ_{Ga}^{II} and μ_{Ga}^I , leaving behind a stable $c(8 \times 2)$ surface.

Theoretical boundary trajectories $r_I(t)$ and $r_{II}(t)$ can be readily computed from Eq. (1) when turning the As flux on or off (see Appendix B), and are displayed in Fig. 4(c). An animation showing the evolving $\mu_{\text{Ga}}(r, t)$ and the advancing boundaries is also available [40]. When the As flux is first turned on, $\mu_{\text{Ga}}(r, t)$ first crosses μ_{Ga}^I at a large distance from the droplet. At this point, $\mu_{\text{Ga}}(r, t)$ is almost tangential to μ_{Ga}^I and boundary I propagates rapidly with time [Fig. 4(c)]. Eventually, as the boundary approaches the droplet, it encounters a significant gradient in $\mu_{\text{Ga}}(r, t)$ so that the boundary slows down. It gradually converges to a stationary position, determined by the steady state $\mu_{\text{Ga}}(r)$ given by Eq. (2). All of these qualitative characteristics of the calculated boundary trajectories in Fig. 4(c) as As flux is turned on are in excellent agreement with the experimental data in Fig. 4(b).

When As is turned off, it is noticeable from Figs. 4(b) and 4(c) that the As-off trajectories are not time reversals of the As-on trajectories. It can be seen that the overall time scale of the evolution is notably longer, as manifested by the larger τ_{Ga} , which is now $\tau_{\text{Ga}}^0 = 1/(k_r C_{\text{As}}^0)$. This is because the initial disequilibrium between surface and bulk solid is smaller, i.e., the initial rate of GaAs decomposition is smaller than the initial rate of crystal growth when turning the As flux on. In addition, the outgoing boundaries do not accelerate until far from the droplet. This reflects the contrasting geometries of the initial μ_{Ga} profiles when As is turned on or off [cf. Figs. 5(a) and 5(b)]. Note that this slower As-off boundary evolution provides improved time resolution compared with the As-on boundary dynamics when obtaining the μ LEED diffraction patterns contained in Fig. 4(a). Again, the overall simulated behavior of the boundary trajectories when As is turned off [Fig. 4(c)] is in excellent qualitative agreement with experiment [Fig. 4(b)].

Figure 5 explains why the chemical potential resolution increases with distance from the droplet. Consider the chemical potential range $\Delta\mu_{\text{Ga}} = \mu_{\text{Ga}}^I - \mu_{\text{Ga}}^{II}$ which corresponds to the stability of the (3×6) phase. For a given $\mu_{\text{Ga}}(r, t)$, this will correspond to a region in real space $\Delta r = r_{II} - r_I$. For small $\Delta\mu_{\text{Ga}}$ we have $\Delta r = \Delta\mu_{\text{Ga}}/|\partial\mu_{\text{Ga}}/\partial r|$, where $\partial\mu_{\text{Ga}}/\partial r$ is the gradient within Δr . At As-on steady state, this region lies close to the droplet, and the steep gradient gives a narrow Δr , as observed in Fig. 5(a). Such a spatially narrow ring is difficult to fully resolve with μ LEED. However, by observing DEPPs before steady state is attained, the lower μ_{Ga} gradient associated with incoming or outgoing boundaries when As is turned on or off translates into a wider Δr in real space [see Figs. 5(a) and 5(b)], thus improving the resolution. This explains why improved phase discrimination occurs when the illumination aperture is placed at a position away from the droplet, as indicated in Fig. 3(a). We may therefore utilize the time dependence of the adatom concentration to control the chemical potential gradient, and hence improve the resolution of the DEPP technique.

C. Mapping the surface phase diagram of GaAs(001) using time-dependent DEPPs

To further elucidate the structure of boundary I we can now utilize the time dependence of the DEPP technique and image the phase pattern at an optimal position on the

trail to improve the chemical potential resolution. This can be combined with selected energy dark-field (SEDF) LEEM [12] which combines dark-field images obtained at optimal incident electron energies and assigns colors to phase-specific intensities, thereby providing a composite phase map [12]. Figure 6(a) displays such a map where blue, green, orange, and yellow correspond to $\beta 2(2 \times 4)$, (3×6) , (6×6) , and $c(8 \times 2)$ phases, respectively. This map has been obtained following the As flux being turned on as the phase boundaries move towards the droplet. This position optimally reveals the sequential order of the phases and also clearly resolves boundary I in more detail, showing a stable (6×6) region and phase intermixing between the (6×6) and $c(8 \times 2)$ phases. In this section we show how such information can provide important insight into the GaAs(001) phase diagram.

GaAs(001) is a classic system which exhibits many surface reconstructions [13–25]. This is because the stoichiometry of the surface is sensitive to experimental conditions. In attempting to understand the surface energetics of various phases, it is customary to evaluate the zero-temperature enthalpies of structures using DFT, and plot these against Ga chemical potential μ_{Ga} (see, for example, [13,26,27,41]). An example of such a phase diagram is contained in Fig. 6(b) [13,23]. The aim is then to relate μ_{Ga} to experimental conditions [26]. However, the fine control of μ_{Ga} in conventional experiments is difficult due to the sensitivity of chemical potential to temperature and deposition. In addition, uncertainty as to whether surfaces have attained equilibrium due to kinetic limitations is also a major limiting factor [13]. The DEPPs contained in Figs. 1 and 6(a) are associated with a continuous and monotonically decreasing μ_{Ga} [39] and so are eminently suitable for carefully exploring μ_{Ga} phase space. As we will now demonstrate, this can provide important information on surface free energy and resolve key issues in GaAs(001) surface thermodynamics.

The (6×6) phase observed in Fig. 6(a) is highly controversial [13,17,21,25,41,42]. While the structure can be readily prepared [13], the energetics are poorly understood [21,41,42]. Using DFT calculations [41], a (12×6) variant of the so-called Kocan model [43] has been shown to have the lowest energy compared with other structural models proposed to date. However, this model was found to be unstable compared to $c(8 \times 2)$ [13,41] (see also [21]). It has therefore been speculated that the (6×6) phase is metastable [42], especially since it has never previously been seen under As flux [13].

Our results provide compelling evidence that the (6×6) phase is indeed stable, and not just metastable. Typically, a metastable phase will only show up when sweeping μ_{Ga} in one direction. However, the (6×6) phase is observed both in diffraction and real space during the droplet trail experiments in Fig. 3 when As is turned on and off. Indeed we see the same sequence of phases at a given location, including (6×6) , whether μ_{Ga} is increasing or decreasing with time.

Figure 6(a) suggests that at high μ_{Ga} (6×6) transforms to $c(8 \times 2)$ via a region of phase coexistence between (6×6) and $c(8 \times 2)$ [44]. Additional experiments, confirming the reversibility of the transition between (6×6) and $c(8 \times 2)$ phases, will be reported in a future publication [45]. At lower Ga chemical potential (6×6) transforms to a (3×6) phase

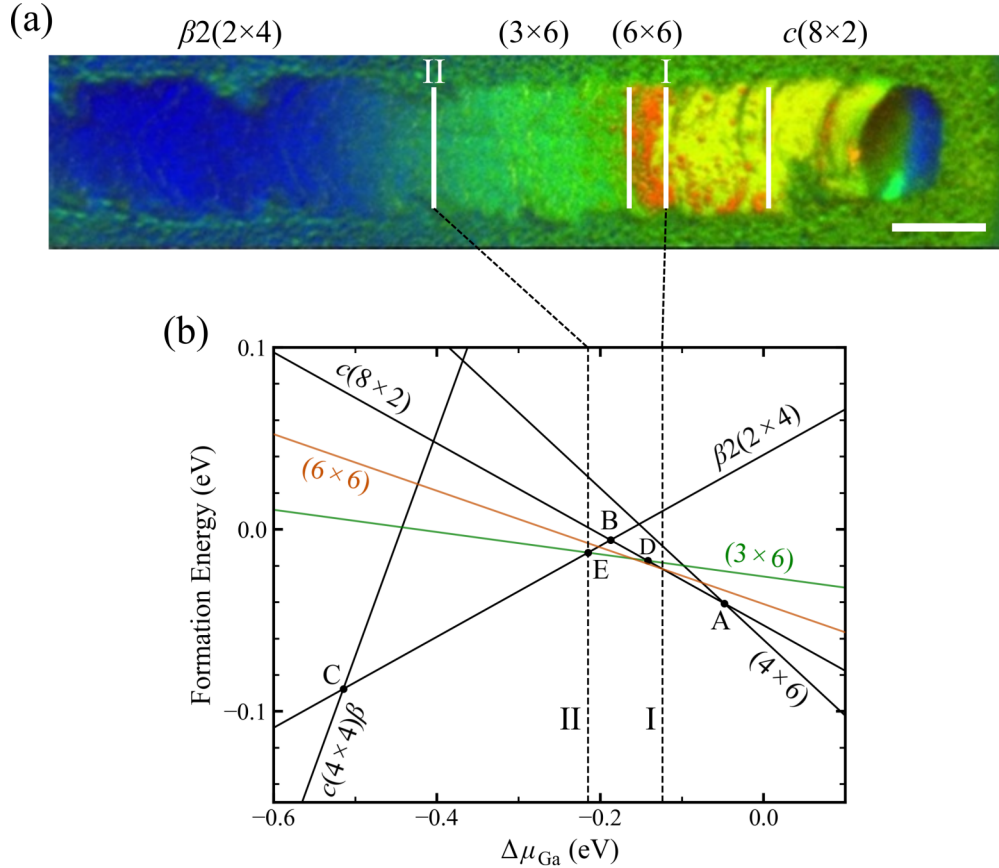


FIG. 6. (a) SEDF LEEM image where blue, green, orange, and yellow correspond to $\beta 2(2 \times 4)$, (3×6) , (6×6) , and $c(8 \times 2)$ phases, respectively (see [12]). This map clearly resolves boundary I in more detail, revealing a stable (6×6) region and phase intermixing between the (6×6) and $c(8 \times 2)$ phases. (b) Existing DFT calculation of the GaAs (001) phase diagram (black lines) [13,23], plotting formation energy with respect to the $\alpha 2(2 \times 4)$ surface per (1×1) unit cell against relative Ga chemical potential $\Delta \mu_{\text{Ga}}$ with respect to Ga bulk at 0 K. From the image in (a) we can schematically superimpose the formation energy lines of the (3×6) and (6×6) phases as shown, to suggest a surface phase diagram at 530 °C. The dashed vertical lines are the chemical potential values defining boundaries I and II. The scale bar in (a) is 2 μm .

[Fig. 6(a)]. This (3×6) phase is stable over a relatively large range of μ_{Ga} and yet has not received wide attention in the literature. In particular, no detailed model has been proposed for this structure. Instead, a wide variety of reconstructions based around $(n \times 6)$ periodicities have been discussed (see, for example, [13,17,21]). One possibility is that the many phases reported may not have attained equilibrium which is based around a (3×6) periodicity as displayed in Fig. 6(a). The diffraction spots of the (3×6) phase corresponding to the $\times 3$ direction become slightly asymmetric with varying incident electron-beam energy, suggesting the phase may exhibit some structural/stoichiometric disorder. It is likely that other phase variants have similar free energies as a function of μ_{Ga} which may explain the wide ranging observations in the literature. At lower μ_{Ga} , it can be seen that the (3×6) phase converts to the well-known $\beta 2(2 \times 4)$ structure [Fig. 6(a)].

The radial sequence of phases observed in the DEPP [Figs. 1 and 6(a)] directly reveals the sequence of phases occurring as a function of μ_{Ga} . With this information, we can superimpose these phases on DFT phase diagrams via Eq. (3). Consider first the (3×6) phase. Since no (4×6) or

$\beta 2(2 \times 4)$ structures exist on the high μ_{Ga} side, its free-energy line must intersect $c(8 \times 2)$ somewhere between A and B in Fig. 6(b). We choose a reasonable point to illustrate, and label it D. Similarly, at lower μ_{Ga} , the phase transforms to $\beta 2(2 \times 4)$ with no $c(4 \times 4)\beta$ or $c(8 \times 2)$ phases visible. The (3×6) free-energy line must therefore intersect $\beta 2(2 \times 4)$ somewhere between B and C. We label this point E. It is therefore possible to approximately superimpose the (3×6) free-energy line on the phase diagram [Fig. 6(b)] as shown. Similarly, the (6×6) phase lies in between $c(8 \times 2)$ and (3×6) . It must therefore intersect with (3×6) between points D and E, and cross $c(8 \times 2)$ between points A and D, allowing us to approximately add the (6×6) free-energy line to the DFT calculation as shown in Fig. 6(b).

Finally, it is important to directly address the apparent discrepancy between our results and published calculations of surface energy. Figures 6(a) and 4(b) show a sequence of phases $\beta 2(2 \times 4) \rightarrow (3 \times 6) \rightarrow (6 \times 6) \rightarrow c(8 \times 2)$ with increasing μ_{Ga} , while theoretical calculations show $\beta 2(2 \times 4) \rightarrow c(8 \times 2)$ [13,23]. Variants of the (6×6) structure have been investigated in detail using DFT [13,41]. However, all structures considered to date have a higher energy than

$\beta 2(2 \times 4)$ or $c(8 \times 2)$ for all μ_{Ga} . Of course, the calculations are based on DFT at $T = 0$ K, while the experiments are at temperatures ~ 550 °C. Therefore it is natural to consider whether entropy could stabilize the (6×6) phase [41]. This is known to occur for Si(111), where at high temperature there is a transition from the much-studied (7×7) structure to a disordered adatom structure [46]. For GaAs(001), the most favorable (6×6) -like structure calculated at $T = 0$ K is (12×6) [41]. However, the proposed structure [41] has the same slope (composition) as $c(8 \times 2)$ and so cannot be the final answer. In particular, Fig. 6 constrains the slope of (6×6) to be less Ga-rich than the proposed (12×6) so that it can intersect $c(8 \times 2)$ and (3×6) appropriately. Nevertheless, the (12×6) DFT calculations indicate that analogous structures would need to lose roughly 50 meV of free energy per (1×1) cell to become stable (see Ref. [41]). Candidate structures already include some elements such as As-Ga dimers and missing As-As dimers that provide configurational entropy [13,41]. At elevated temperatures we could also imagine Ga adatoms playing a role, providing additional flexibility in satisfying electron-counting heuristics. With $kT \sim 70$ meV, it seems reasonable to envisage that such structural elements could contribute sufficient configurational entropy to stabilize (6×6) . In addition, elevated temperatures provide thermal expansion and lowering of elastic stiffness. For structures with dimers, one cannot rule out that this may also lower free energies compared with $T = 0$ K.

While extensive DFT calculations for (3×6) structures are presently unavailable, it would appear that configurational entropy will also play a significant role in stabilizing the phase. As discussed earlier, disordered elements are suggested by the diffraction data. It is therefore conceivable that thermal effects associated with a basic (3×6) unit cell represents the ground state of the $(n \times 6)$ structures observed throughout the literature [13,17,21]. In any event, the information contained in Fig. 6 provides an important foundation for proposing atomistic models of the $(n \times 6)$ and (6×6) phases.

IV. CONCLUSION

In summary, we have combined LEEM imaging and μ LEED techniques to map surface phases around liquid Ga droplets during droplet epitaxy. This can be used to approximately map the GaAs(001) phase diagram and is highly complementary to existing DFT calculations. The method reflects phase stability at finite temperature and so naturally incorporates the influence of entropy. We envisage DEPPs will be used to map surface free energy for a wide range of technologically important III-V materials, including nitrides.

Information on the data that underpins the results presented here, including how to access them, can be found in the Cardiff University data catalog [47].

ACKNOWLEDGMENTS

We are grateful to W.-X. Tang and Z. Zhou for helpful discussions during the early stages of this project. The authors acknowledge support from EPSRC research Grants No. EP/P023452/1 and No. EP/N022661/1. This project also has

received funding from the European Union's Horizon 2020 research and innovation program under Marie Skłodowska-Curie Grant Agreement No. 701246.

APPENDIX A: SOLVING THE STEADY-STATE REACTION-DIFFUSION EQUATION

The Ga reaction-diffusion equation is a boundary value problem (BVP) given by

$$\frac{\partial C_{\text{Ga}}}{\partial t} = D_{\text{Ga}} \left(\frac{\partial^2 C_{\text{Ga}}}{\partial r^2} + \frac{1}{r} \frac{\partial C_{\text{Ga}}}{\partial r} \right) - k_r [C_{\text{Ga}} C_{\text{As}} - (C_{\text{Ga}} C_{\text{As}})_{eq}], \quad (\text{A1})$$

for $t > 0$ and $r_D < r < L$. At $r = r_D$ we set the boundary condition

$$-D_{\text{Ga}} \frac{\partial C_{\text{Ga}}}{\partial r} \Big|_{r=r_D} = k_D (C_{\text{Ga}}^l - C_{\text{Ga}} \Big|_{r=r_D}), \quad (\text{A2})$$

where k_D is a rate constant associated to Ga adatom attachment to the droplet. Equation (A2) reflects conservation of mass for Ga transport across the contact line. In the limit of fast attachment/detachment compared to adatom diffusion (A2) becomes

$$C_{\text{Ga}} \Big|_{r=r_D} = C_{\text{Ga}}^l. \quad (\text{A3})$$

At $r = L$ the boundary condition ought to reflect zero net Ga transport, and thus we have

$$\frac{\partial C_{\text{Ga}}}{\partial r} \Big|_{r=L} = 0. \quad (\text{A4})$$

The steady-state form of (A1) is

$$\frac{d^2 C_{\text{Ga}}}{d \rho^2} + \frac{1}{\rho} \frac{d C_{\text{Ga}}}{d \rho} - C_{\text{Ga}} + \frac{(C_{\text{Ga}} C_{\text{As}})_{eq}}{F_{\text{As}} \tau_{\text{As}}} = 0, \quad (\text{A5})$$

where $C_{\text{As}} = F_{\text{As}} \tau_{\text{As}}$ has been introduced, and ρ is the natural radial coordinate

$$\rho \equiv \frac{r}{L_{\text{Ga}}}, \quad (\text{A6})$$

which spans from $\rho_D \equiv r_D/L_{\text{Ga}}$ to $\rho_L \equiv L/L_{\text{Ga}}$. The general solution to (A5) is

$$C_{\text{Ga}}(\rho) = AI_0(\rho) + BK_0(\rho) + \frac{(C_{\text{Ga}} C_{\text{As}})_{eq}}{F_{\text{As}} \tau_{\text{As}}}, \quad (\text{A7})$$

where I_0 and K_0 are the modified Bessel functions of zeroth order, and A and B are arbitrary constants. Imposing the boundary conditions of (A3) and (A4) yields $A \rightarrow 0$ (for $L \gg L_{\text{Ga}}, r_D$), while B is simply

$$B = \frac{C_{\text{Ga}}^l - C_{\text{Ga}}^L}{K_0(\rho_D)}, \quad (\text{A8})$$

where $C_{\text{Ga}}^L \equiv (C_{\text{Ga}} C_{\text{As}})_{eq}/(F_{\text{As}} \tau_{\text{As}})$. Therefore, the As-on steady-state Ga concentration profile is

$$C_{\text{Ga}}(r) = BK_0(r/L_{\text{Ga}}) + \frac{(C_{\text{Ga}} C_{\text{As}})_{eq}}{F_{\text{As}} \tau_{\text{As}}}, \quad (\text{A9})$$

with B given by (A8).

APPENDIX B: SOLVING THE TIME-DEPENDENT REACTION-DIFFUSION EQUATION

Using the standard results of Sturm-Liouville theory (see, for example, Ref. [48]), it can be shown that the solution to the BVP defined by (A1), (A3), and (A4) can be written as

$$C_{\text{Ga}}(r, t) = C_{\text{Ga}}^{ss}(r) + \sum_{n=1}^{\infty} c_n^0 \exp(-a_n t / \tau_{\text{Ga}}) \phi_n(r / L_{\text{Ga}}), \quad (\text{B1})$$

where $C_{\text{Ga}}^{ss}(r)$ is the steady-state solution to the BVP, a_n (with $n = 1, 2, \dots, \infty$) are eigenvalues, $\phi_n(\rho)$ are eigenfunctions, and c_n^0 are coefficients associated to the initial C_{Ga} profile.

The eigenvalues are the roots to characteristic equation

$$J_0(\lambda_n \rho_D) Y_1(\lambda_n \rho_L) - J_1(\lambda_n \rho_L) Y_0(\lambda_n \rho_D) = 0, \quad (\text{B2})$$

where $\lambda_n \equiv \sqrt{a_n - 1}$, and J_v and Y_v are the Bessel functions of the first and second kind, respectively, of order v . The associated eigenfunctions are

$$\phi_n(\rho) = k_n [Y_0(\lambda_n \rho_D) J_0(\lambda_n \rho) - J_0(\lambda_n \rho_D) Y_0(\lambda_n \rho)], \quad (\text{B3})$$

where k_n are normalization constants containing λ_n , ρ_D , and ρ_L .

Note that the eigenvalues a_n and eigenfunctions ϕ_n (as well as reaction time τ_{Ga} and length L_{Ga}) are different for the As-on versus the As-off problem, as the C_{As} of (A1) is either $F_{\text{As}} \tau_{\text{As}}$ or C_{As}^0 , respectively. Also note that $C_{\text{Ga}}^{ss}(r)$ is given by (A9) for the As-on problem, but C_{Ga}^l for the As-off problem.

To numerically evaluate our time-dependent Ga concentration profiles, it is sufficient to assign values to concentrations C_{Ga}^l and $C_{\text{Ga}}^L = (C_{\text{Ga}} C_{\text{As}})_{eq} / (F_{\text{As}} \tau_{\text{As}})$, and to the radial coordinates ρ_D and ρ_L .

-
- [1] N. Koguchi, S. Takahashi, and T. Chikyow, *J. Cryst. Growth* **111**, 688 (1991).
- [2] M. Gurioli, Z. Wang, A. Rastelli, T. Kuroda, and S. Sanguinetti, *Nat. Mater.* **18**, 799 (2019).
- [3] J. Wu and Z. M. Wang, *J. Phys. D: Appl. Phys.* **47**, 173001 (2014).
- [4] J. H. Lee, Z. M. Wang, Z. Y. AbuWaar, and G. J. Salamo, *Cryst. Growth Des.* **9**, 715 (2009).
- [5] M. Yamagawa, T. Mano, T. Kuroda, T. Tateno, K. Sakoda, G. Kido, N. Koguchi, and F. Minami, *Appl. Phys. Lett.* **89**, 113115 (2006).
- [6] S. Huang, Z. Niu, Z. Fang, H. Ni, Z. Gong, and J. Xia, *Appl. Phys. Lett.* **89**, 031921 (2006).
- [7] T. Mano and N. Koguchi, *Proceedings of the 13th International Conference on Molecular Beam Epitaxy* [*J. Cryst. Growth* **278**, 108 (2005)].
- [8] T. Mano, T. Kuroda, S. Sanguinetti, T. Ochiai, T. Tateno, J. Kim, T. Noda, M. Kawabe, K. Sakoda, G. Kido, and N. Koguchi, *Nano Lett.* **5**, 425 (2005).
- [9] C. Somaschini, S. Bietti, N. Koguchi, and S. Sanguinetti, *Appl. Phys. Lett.* **97**, 203109 (2010).
- [10] Z. Gong, Z. C. Niu, S. S. Huang, Z. D. Fang, B. Q. Sun, and J. B. Xia, *Appl. Phys. Lett.* **87**, 093116 (2005).
- [11] C. Somaschini, S. Bietti, N. Koguchi, and S. Sanguinetti, *Nano Lett.* **9**, 3419 (2009).
- [12] Y. R. Niu, J. Pereiro, D. Gomez, and D. E. Jesson, *Ultramicroscopy* **200**, 79 (2019).
- [13] A. Ohtake, *Surf. Sci. Rep.* **63**, 295 (2008).
- [14] V. P. LaBella, M. R. Krause, Z. Ding, and P. M. Thibado, *Surf. Sci. Rep.* **60**, 1 (2005).
- [15] B. A. Joyce and D. D. Vvedensky, *Mat. Sci. Eng. R* **46**, 127 (2004).
- [16] Q. Xue, T. Hashizume, J. M. Zhou, T. Sakata, T. Ohno, and T. Sakurai, *Phys. Rev. Lett.* **74**, 3177 (1995).
- [17] J. G. McLean, P. Kruse, and A. C. Kummel, *Surf. Sci.* **424**, 206 (1999).
- [18] S.-H. Lee, W. Moritz, and M. Scheffler, *Phys. Rev. Lett.* **85**, 3890 (2000).
- [19] A. Ohtake, S. Tsukamoto, M. Pristovsek, N. Koguchi, and M. Ozeki, *Phys. Rev. B* **65**, 233311 (2002).
- [20] A. Ohtake, J. Nakamura, S. Tsukamoto, N. Koguchi, and A. Natori, *Phys. Rev. Lett.* **89**, 206102 (2002).
- [21] M. Pristovsek, S. Tsukamoto, A. Ohtake, N. Koguchi, B. G. Orr, W. G. Schmidt, and J. Bernholc, *Phys. Status Solidi B* **240**, 91 (2003).
- [22] E. Penev, P. Kratzer, and M. Scheffler, *Phys. Rev. Lett.* **93**, 146102 (2004).
- [23] A. Ohtake, P. Kocán, K. Seino, W. G. Schmidt, and N. Koguchi, *Phys. Rev. Lett.* **93**, 266101 (2004).
- [24] M. Takahasi and J. Mizuki, *Phys. Rev. Lett.* **96**, 055506 (2006).
- [25] A. Ohtake, *Phys. Rev. B* **75**, 153302 (2007).
- [26] B. Meyer, in *Computational Nanoscience: Do It Yourself! (NIC Series)*, edited by J. Grotendorst, S. Blugel, and D. Marx (John von Neumann Institute for Computing, Jülich, 2006), Vol. 31, pp. 411–418.
- [27] J. Y. Tsao, *Materials Fundamentals of Molecular Beam Epitaxy* (Academic, San Diego, 1993).
- [28] J. Tersoff, D. E. Jesson, and W. X. Tang, *Science* **324**, 236 (2009).
- [29] Z. Y. Zhou, C. X. Zheng, W. X. Tang, D. E. Jesson, and J. Tersoff, *App. Phys. Lett.* **97**, 121912 (2010).
- [30] C. X. Zheng, J. Tersoff, W. X. Tang, A. Morreau, and D. E. Jesson, *Phys. Rev. B* **93**, 195314 (2016).
- [31] D. E. Jesson and W. X. Tang, in *Microscopy* edited by A. Mendez-Vilas and J. Diaz (Formatex, Badajoz, 2010).
- [32] P. J. Timans, *J. Appl. Phys.* **72**, 660 (1992).
- [33] E. Hilner, A. A. Zakharov, K. Schulte, P. Kratzer, J. N. Andersen, E. Lundgren, and A. Mikkelsen, *Nano Lett.* **9**, 2710 (2009).
- [34] C. Zheng, W.-X. Tang, and D. E. Jesson, *J. Vac. Sci. Technol. A* **34**, 043201 (2016).
- [35] E. Bauer, *Surface Microscopy with Low Energy Electrons* (Springer-Verlag, New York, 2014).
- [36] Z. Y. Zhou, C. X. Zheng, W. X. Tang, J. Tersoff, and D. E. Jesson, *Phys. Rev. Lett.* **111**, 036102 (2013).
- [37] F. W. J. Olver and L. C. Maximon, in *NIST Handbook of Mathematical Functions*, edited by F. W. J. Olver, D. W. Lozier, R. F. Boisvert, and C. W. Clark (Cambridge University Press, Cambridge, UK, 2010), Chap. 10.
- [38] J. Tersoff, M. D. Johnson, and B. G. Orr, *Phys. Rev. Lett.* **78**, 282 (1997).

- [39] D. Wall, I. Lohmar, K. R. Roos, J. Krug, M. H. von Hoegen, and F.-J. M. zu Heringdorf, *New J. Phys.* **12**, 103019 (2010).
- [40] See Supplemental Material at <http://link.aps.org/supplemental/10.1103/PhysRevMaterials.3.124603> for a LEEM movie of phase boundary motion dynamics and a theoretical movie simulating the evolving chemical potential in the droplet vicinity when turning the As flux on and off.
- [41] K. Seino, W. G. Schmidt, and A. Ohtake, *Phys. Rev. B* **73**, 035317 (2006).
- [42] M. Kuball, D. T. Wang, N. Esser, M. Cardona, J. Zegenhagen, and B. O. Fimland, *Phys. Rev. B* **51**, 13880 (1995).
- [43] P. Kocán, A. Ohtake, and N. Koguchi, *Phys. Rev. B* **70**, 201303(R) (2004).
- [44] J. B. Hannon, F.-J. Meyer zu Heringdorf, J. Tersoff, and R. M. Tromp, *Phys. Rev. Lett.* **86**, 4871 (2001).
- [45] D. Gomez *et al.* (unpublished).
- [46] Y. Fukaya and Y. Shigeta, *Phys. Rev. Lett.* **85**, 5150 (2000).
- [47] K. Hannikainen, D. Gomez, J. Pereiro, Y. R. Niu, and D. E. Jesson, <http://doi.org/10.17035/d.2019.0090902258>, 2019.
- [48] W. E. Boyce and R. C. DiPrima, *Elementary Differential Equations and Boundary Value Problems*, 10th Edition (Wiley, New York, 2012).